Cycloaddition

Understanding the 1,3-Dipolar Cycloadditions of Allenes

Song Yu,[a] Pascal Vermeeren,[a] Kevin van Dommelen,[a] F. Matthias Bickelhaupt,*[a, b] and Trevor A. Hamlin*[a]

Abstract: We have quantum chemically studied the reactivity, site-, and regioselectivity of the 1,3-dipolar cycloaddition between methyl azide and various allenes, including the archetypal allene propadiene, heteroallenes, and cyclic allenes, by using density functional theory (DFT). The 1,3-dipolar cycloaddition reactivity of linear (hetero)allenes decreases as the number of heteroatoms in the allene increases, and formation of the 1,5-adduct is, in all cases, favored over the 1,4-adduct. Both effects find their origin in the strength of the primary orbital interactions. The cycloaddition reactivity of cyclic allenes was also investigated, and the increased predistortion of allenes, that results upon cyclization, leads to systematically lower activation barriers not due to the expected variations in the strain energy, but instead from the differences in the interaction energy. The geometric predistortion of cyclic allenes enhances the reactivity compared to linear allenes through a unique mechanism that involves a smaller HOMO–LUMO gap, which manifests as more stabilizing orbital interactions.

Introduction

Allenes are a class of unsaturated hydrocarbon that contain two cumulated double bonds and have received significant attention in the past decade due to their privileged role in the synthesis of natural products through cycloaddition reactions.[1] The simplest allene, propadiene (**CCC**), for instance, reacts with both cyclopentadiene and 1,3-dipoles to form either a substituted norbornene[2] or a heterocycle,[3] respectively (Scheme 1 a and b), both of which are common motifs in natural products. Intramolecular Diels–Alder reactions[4] as well as 1,3-dipolar cycloadditions[5] (Scheme 1 c and d) of allenes provide strategies for the construction of complex polycyclic molecules.[6] In addition, the cycloaddition reactivity of allenes can be broadened to heteroallenes, such as ketenimine (**CCN**),[7] ketene (**CCO**),[8] carbodiimide (**NCN**),[9] isocyanate (**NCO**),[10] and even to carbon dioxide (**OCO**).[11]

In contrast, strained allenes, that is, cyclic allenes, have received less attention in the field likely due to their lower kinetic stabilities.[12] Nevertheless, experimental studies have shown that strained allenes can be formed in situ and trapped instantaneously by either dienes or 1,3-dipoles.[13] For example, Houk and co-workers studied the formation and subsequent trapping of 1,2-cyclohexadiene in a Diels–Alder reaction (Scheme 2 a).[13d] Lofstrand et al. synthesized and subsequently trapped 1,2-cyclohexadiene, through a 1,3-dipolar cycloaddition under mild conditions (Scheme 2 b).[13e] Houk and Garg recently carried out a systematic study on the synthesis of azacyclic allenes as well as their reactivity towards cycloadditions (Scheme 2 c).[13g] These examples clearly illustrate that cyclic allenes can serve as prominent building blocks in the construction of polycyclic compounds and may also engage in rapid reactions in analogy with strained alkenes and alkynes.[14]

A number of theoretical studies have shed light on the cycloaddition reactivity of allenes. A concerted asynchronous mechanism has been proposed to be a more energetically favorable reaction pathway for cycloadditions of allenes.[13g, 15] Gandolfi and co-workers proposed that the differences in the extent of structural deformations determine the trends in reaction barrier heights of the cycloadditions of allenes.[15a,b] On the contrary, an activation strain analysis on transition structures, by Garg and co-workers, concluded just the opposite, namely, that the strength of the interaction plays a large role in determining the regioselectivity of the Diels–Alder reactions of azacyclic allenes.[13g] To the best of our knowledge, a thorough investigation into the reactivity, site-, and regioselectivity of cycloadditions of allenes has not yet been reported.

[a] S. Yu, P. Vermeeren, K. van Dommelen, Prof. Dr. F. M. Bickelhaupt, Dr. T. A. Hamlin
Department of Theoretical Chemistry
Amsterdam Institute of Molecular and Life Sciences (AIMMS)
Amsterdam Center for Multiscale Modeling (ACMM)
Vrije Universiteit Amsterdam
De Boelelaan 1083, 1081 HV Amsterdam (The Netherlands)
E-mail: f.m.bickelhaupt@vu.nl
t.a.hamlin@vu.nl

[b] Prof. Dr. F. M. Bickelhaupt
Institute for Molecules and Materials (IMM)
Radboud University
Heyendaalseweg 135, 6525 AJ Nijmegen (The Netherlands)

Supporting information and the ORCID identification numbers for the authors of this article can be found under: https://doi.org/10.1002/chem.202000857.

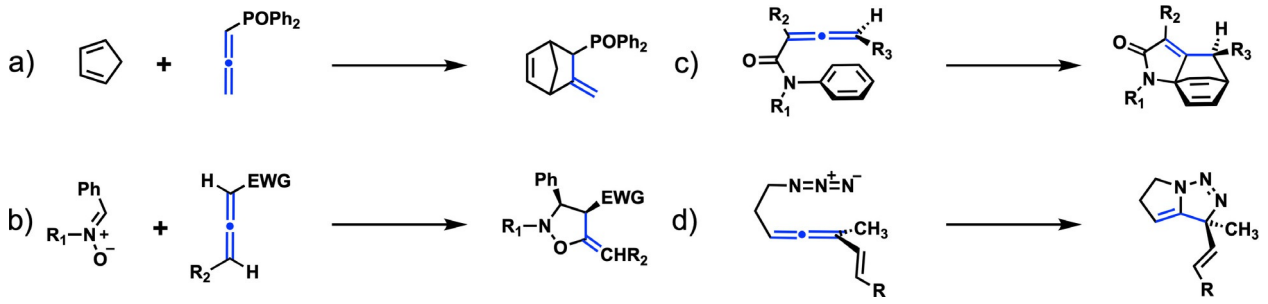

Scheme 1. Inter- and intramolecular Diels–Alder reactions and 1,3-dipolar cycloadditions of propadiene.

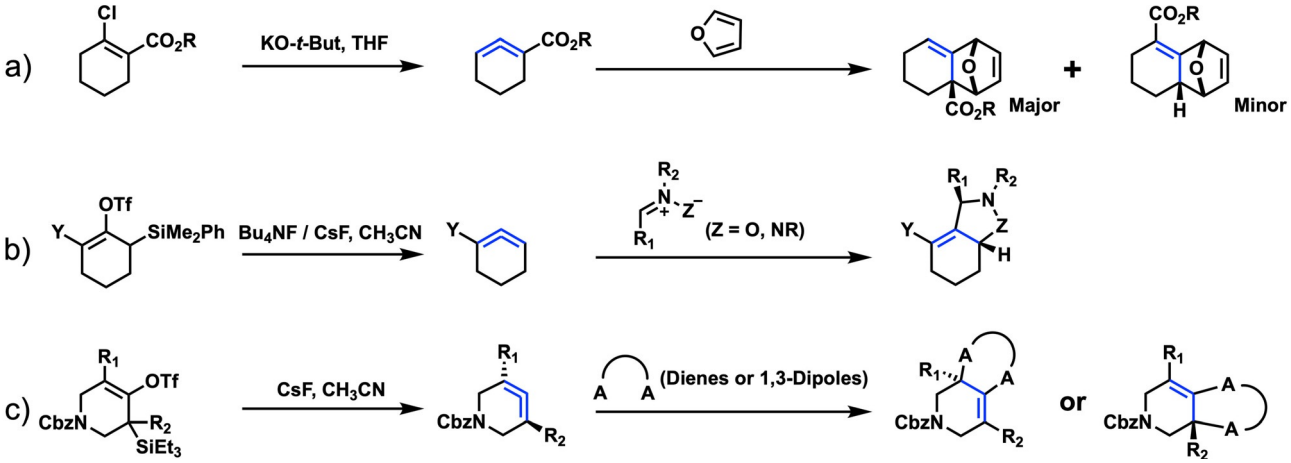

Scheme 2. Diels–Alder reactions and 1,3-dipolar cycloadditions of strained allenes.

We have performed a systematic computational study of the concerted 1,3-dipolar cycloaddition reactions of allenes, including the linear (hetero)allenes propadiene (**CCC**; **L3**), ketenimine (**CCN**), ketene (**CCO**), carbodiimide (**NCN**), isocyanate (**NCO**), and carbon dioxide (**OCO**) and a series of cyclic allenes 1,2-cyclooctadiene (**C8**), 1,2-cycloheptadiene (**C7**), and 1,2-cyclohexadiene (**C6**). These cyclic allenes have all been synthesized[16] and might be relevant reactive dienophiles/dipolarophiles in bioorthogonal chemistries in the future.[17] As azides are common reactants in 1,3-dipolar cycloadditions,[18] as well as strain-promoted azide–alkyne cycloadditions (SPAACs),[14a-c] methyl azide (**Az**) was chosen as the model 1,3-dipole in this study. The activation strain model (ASM)[19] in combination with quantitative Kohn–Sham molecular orbital (KS-MO) theory and the matching energy decomposition analysis (EDA)[20] were employed to provide insight into the factor controlling the reactivity in these cycloaddition reactions. This approach has proven valuable for understanding of the reactivity of related pericyclic reactions and continues our current research line into the reactivity of cyclic dienophiles and dipolarophiles.[21]

Computational Methods

All calculations were carried out in ADF2017,[22] using the BP86[23] functional with the TZ2P basis set.[24] The exchange-correlation (XC) functional has been proven to be accurate in calculating the relative trends in activation and reaction energies for cycloadditions.[25] Additionally, single-point energies were computed at BP86-D3(BJ)/TZ2P,[26] M06-2X/TZ2P,[27] and COSMO(toluene)BP86/TZ2P[28] on the fully optimized BP86/TZ2P geometries in order to assess the effect of a meta-hybrid functional, dispersion-corrections, and solvation on the computed reactivity trends. Frequency calculations were performed in order to characterize the nature of the stationary points. Local minima present only real frequencies, whereas transition state structures have one imaginary frequency. The potential energy surface (PES) was calculated using the intrinsic reaction coordinate (IRC) method, which follows the imaginary eigenvector of the transition structure towards the reactant and product. The resulting PES was analyzed with the aid of the PyFrag 2019 program.[29] All chemical structures were illustrated using CYLview.[30]

Quantitative analyses of the activation barriers associated with the studied reactions are obtained by means of the activation strain model (ASM) of reactivity.[19] Herein, the PES, $\Delta E(\zeta)$, is decomposed into the strain energy, $\Delta E_{strain}(\zeta)$, and the interaction energy, $\Delta E_{int}(\zeta)$ [Eq. (1)]. All energy terms are projected onto the reaction coordinate ζ, the average distance of newly forming bonds, which undergoes a well-defined change during the course of the reactions and has been proven to provide reliable results for cycloaddition reactions.[21a,25b,c,31]

$$\Delta E(\zeta) = \Delta E_{strain}(\zeta) + \Delta E_{int}(\zeta) \quad (1)$$

The $\Delta E_{strain}(\zeta)$ is associated with the rigidity as well as the structural deformation of the reactants from their equilibrium geometry to the geometry acquired along the reaction coordinate. The total $\Delta E_{strain}(\zeta)$ can be further divided into the strain energy associated with deforming each respective reactant [Eq. (2)].

$$\Delta E_{strain}(\zeta) = \Delta E_{strain,reactant,A}(\zeta) + \Delta E_{strain,reactant,B}(\zeta) \quad (2)$$

The $\Delta E_{int}(\zeta)$ is related to the electronic structure of the reactants and their spatial orientation and takes the mutual interaction between the deformed reactants into account. In order to obtain a deeper insight into the physical mechanism behind the interaction energy, we employ the canonical energy decomposition analysis (EDA).[20] This analysis method decomposes the interaction energy between the two deformed reactants, within the framework of Kohn–Sham DFT, into three physically meaningful terms [Eq. (3)].

$$\Delta E_{int}(\zeta) = \Delta V_{elstat}(\zeta) + \Delta E_{Pauli}(\zeta) + \Delta E_{oi}(\zeta) \quad (3)$$

The electrostatic interaction, $\Delta V_{elstat}(\zeta)$, corresponds to the classical electrostatic interaction between the unperturbed charge distributions of the deformed reactants. The Pauli repulsion, $\Delta E_{Pauli}(\zeta)$, comprises the repulsion between closed-shell occupied orbitals and is, therefore, destabilizing. The orbital interaction, $\Delta E_{oi}(\zeta)$, accounts for the stabilizing orbital interactions such as electron-pair bonding, charge transfer (interaction between the occupied orbitals of fragment A with the unoccupied orbitals of fragment B, and vice versa), and polarization (e.g., occupied-unoccupied orbital mixing on fragment A due to the presence of fragment B and vice versa). A detailed step-by-step protocol on how to perform the activation strain and energy decomposition analysis can be found in ref. [19a].

The magnitude of the orbital interaction of a 1,3-dipolar cycloaddition mainly comes from two distinct orbital interaction mechanisms, namely, the normal electron demand (NED) interaction, occurring between occupied orbitals of the dipole and unoccupied orbitals of the dipolarophile (the allene in this study), and the inverse electron demand (IED) interaction, originating from the interaction between the unoccupied orbitals of the dipole with occupied orbitals of the dipolarophile. The stabilization of a specific orbital interaction mechanism is proportional to the orbital overlap squared divided by their respective orbital energy gap, that is, $S^2/\Delta\varepsilon$.[32] Thus, with the help of this relation, we can quantify the importance of the individual orbital interaction mechanisms.

The atomic charge distribution was analyzed by using the Voronoi deformation density (VDD) method.[33] The VDD method partitions the space into so-called Voronoi cells, which are non-overlapping regions of space that are closer to nucleus A than to any other nucleus. The charge distribution is determined by taking a fictitious promolecule as reference point, in which the electron density is simply the superposition of the atomic densities. The change in density in the Voronoi cell when going from this promolecule to the final molecular density of the interacting system is associated with the VDD atomic charge Q. The VDD atomic charge Q_A of atom A is calculated according to Equation (4):

$$Q_A^{VDD} = -\int_{\text{Voronoi cell of A}} [\rho(r) - \rho_{promolecule}(r)]dr \quad (4)$$

So, instead of computing the amount of charge contained in an atomic volume, we compute the flow of charge from one atom to the other upon formation of the molecule. The physical interpretation is therefore straightforward. A positive atomic charge Q_A corresponds to the loss of electrons, whereas a negative atomic charge Q_A is associated with the gain of electrons in the Voronoi cell of atom A.

Results and Discussion

1,3-Dipolar cycloadditions of linear allenes

As a starting point, we studied the 1,3-dipolar cycloaddition reaction between methyl azide (**Az**) and the following linear (hetero)allenes: propadiene (**CCC**), ketenimine (**CCN**), ketene (**CCO**), carbodiimide (**NCN**), isocyanic acid (**NCO**), and carbon dioxide (**OCO**). For each 1,3-dipolar cycloaddition, two regiospecific cycloadducts can be formed, the 1,5-adduct with the methyl group adjacent to the second double bond and the 1,4-adduct with them on opposite sides (Scheme 3). Additionally, the asymmetric heteroallenes **CCN**, **CCO**, and **NCO** are able to form two site-specific adducts, i.e., coordinating with either of the two double bonds.

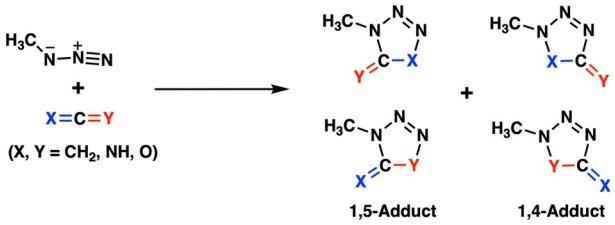

Scheme 3. The 1,3-dipolar cycloaddition between **Az** and a linear allene.

Table 1 lists the activation energies, $\Delta E^{\ddagger}$, and reaction energies, ΔE_{rxn}, for the studied 1,3-dipolar cycloadditions between **Az** and linear (hetero)allenes. Three clear trends can be observed. In the first place, the cycloadditions towards the 1,5-adducts are kinetically and thermodynamically favored over the formation of the 1,4-adducts. Secondly, for the asymmetric heteroallenes, **Az** preferentially attacks at the more electropositive of the two terminal atoms. The only exception, however, is **CCO**, which has a *slightly* lower $\Delta E^{\ddagger}$ for the attack at the CO (19.2 kcal mol^{-1}) than the CC (20.0 kcal mol^{-1}). Thirdly, the cycloaddition reactivity decreases when heteroatoms are introduced in the linear allene, from **CCC** to **CCN** and **CCO**, as well as from **CCO** to **NCO** to **OCO** and from **CCN** to **NCN**. The computed trends in reactivity at BP86/TZ2P agree well with those

Table 1. Electronic reaction barriers $\Delta E^{\ddagger}$ and reaction energies ΔE_{rxn} [kcal mol^{-1}] for the 1,3-dipolar cycloadditions between **Az** and linear allenes leading to 1,4- and 1,5-adducts computed at various levels of theory.[d]

Allene	Site	1,5-Adduct						1,4-Adduct					
		$\Delta E^{\ddagger}$[a]	$\Delta E^{\ddagger}$[b]	$\Delta E^{\ddagger}$[c]	ΔE_{rxn}[a]	ΔE_{rxn}[b]	ΔE_{rxn}[c]	$\Delta E^{\ddagger}$[a]	$\Delta E^{\ddagger}$[b]	$\Delta E^{\ddagger}$[c]	ΔE_{rxn}[a]	ΔE_{rxn}[b]	ΔE_{rxn}[c]
OCO		32.1	28.8	35.8	20.6	17.2	14.8	53.8	50.6	62.6	37.8	34.8	35.7
NCN		28.0	23.7	30.9	−15.3	−19.8	−25.2	35.8	31.6	43.5	1.6	−2.6	−6.6
NCO	CO	27.9	24.1	28.8	14.6	10.7	8.3	45.0	41.4	54.0	32.4	29.0	27.0
	NC	26.4	22.7	28.9	−14.9	−18.8	−24.0	42.8	39.0	50.8	6.6	2.9	−0.1
CCO	CO	19.2	15.0	21.7	3.5	−0.8	−2.6	27.1	23.4	40.2	16.5	12.9	11.5
	CC	20.0	15.7	26.2	−32.2	−36.4	−42.1	29.1	24.8	37.2	−24.5	−28.6	−32.2
CCN	CN	22.6	18.0	27.1	−20.3	−25.1	−29.1	26.4	22.2	34.3	−6.1	−10.4	−13.7
	CC	20.0	15.7	27.0	−30.8	−35.6	−41.3	23.5	19.0	30.8	−28.1	−32.6	−36.7
CCC		19.0	14.1	24.4	−34.0	−39.1	−43.7	19.5	14.8	25.2	−31.5	−36.2	−39.7

[a] Computed at BP86/TZ2P. [b] Computed at BP86-D3(BJ)/TZ2P//BP86/TZ2P. [c] Computed at M06-2X/TZ2P//BP86/TZ2P. [d] See Table S1 for computed enthalpies and Gibbs free energies.

calculated at BP86-D3(BJ)/TZ2P//BP86/TZ2P and M06-2X/TZ2P//BP86/TZ2P. We note that, when using M06-2X/TZ2P//BP86/TZ2P, the two site-selective cycloadditions of **NCO**, forming the 1,5-adduct, have nearly identical reaction barriers. Furthermore, the observed trends in reactivity, site-, and regioselectivity also hold when solvent effects in toluene are included at COSMO(toluene)BP86/TZ2P//BP86/TZ2P (Table S1 in the Supporting Information).

1,5- versus 1,4-regioselectivity

Next, we turn to the activation strain model (ASM)[19] of reactivity to gain a quantitative insight into the physical factors governing the 1,5- versus 1,4-regioselectivity in the 1,3-dipolar cycloadditions presented herein. In Figure 1, we focus on the ASM diagram for the 1,5- vs. 1,4-regioselectivity of **OCO** for which the difference in $\Delta E^{\ddagger}$ is the largest (Table 1). The ASM diagrams of the other linear allenes possess the same characteristics, only less pronounced (Figures S1–S7). The lower $\Delta E^{\ddagger}$ for the formation of the 1,5-adduct originates mainly from a more stabilizing ΔE_{int} term, whereas the ΔE_{strain} is nearly identical (Figure 1 a). The canonical energy decomposition analysis (EDA)[20] reveals that both the more stabilizing ΔV_{elstat} and ΔE_{oi} are the causes of the more favorable ΔE_{int} term for the 1,5-adduct formation compared to the 1,4-adduct (Figure 1 b).

The more stabilizing ΔE_{oi} for the 1,3-dipolar cycloaddition yielding the 1,5-adduct can be entirely described to the more effective orbital overlap of the normal electron demand (NED) interaction occurring between the HOMO−1_{Az} and $LUMO_{oco}$. Only the lower-lying HOMO−1_{Az} participates in the NED interaction, because its lobes are oriented towards the LUMO of **OCO**, while the lobes of $HOMO_{Az}$ are orthogonal to the $LUMO_{oco}$ (Scheme S1). As shown in Scheme 4, the HOMO−1_{Az} has the largest lobe on the nitrogen next to the methyl group, due to a methyl-induced mix of the π-atomic orbitals of the N_3 fragment of **Az** (Scheme S1e). The $LUMO_{oco}$ has a larger lobe on the carbon atom than on the terminal oxygens, due to the more diffuse nature of the 2p atomic orbital of carbon com-

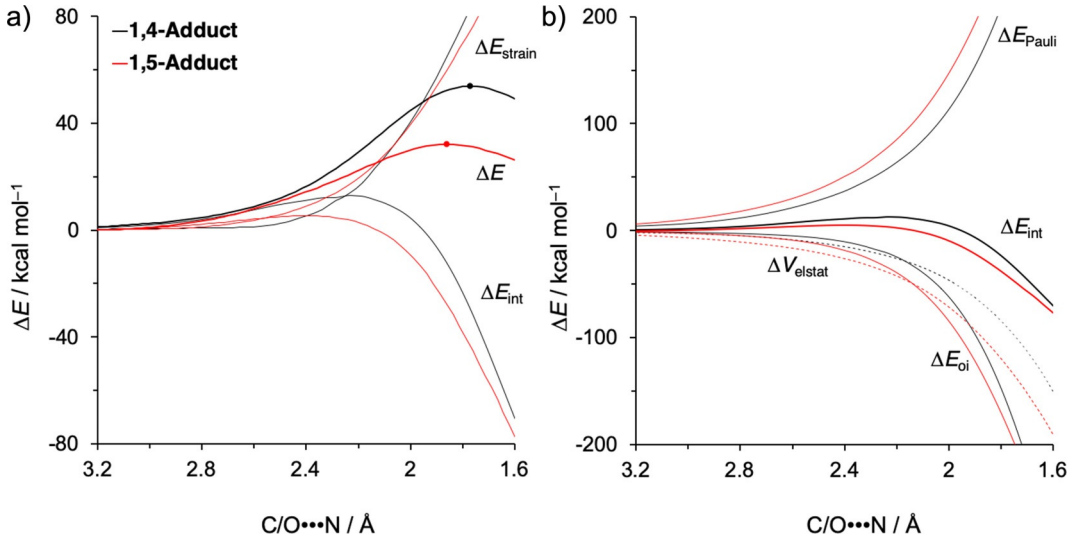

Figure 1. a) Activation strain and b) energy decomposition analysis of the 1,3-dipolar cycloaddition between **Az** and **OCO**, projected onto the average newly forming C/O···N bond, computed at BP86/TZ2P.

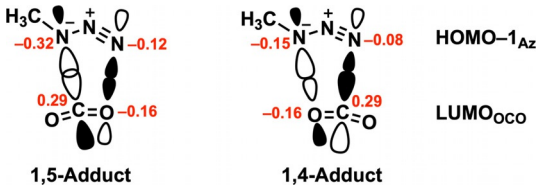

Scheme 4. Schematic diagrams of the orbital interaction between the HOMO−1 of **Az** and the LUMO of **OCO** for the 1,4- and 1,5-adducts. VDD charges (red, in electrons) of key atoms in isolated fragment computed at BP86/TZ2P.

pared to oxygen, which, in turn, leads to a better HOMO−1_{Az}–$LUMO_{OCO}$ orbital overlap when forming the 1,5-adduct compared to the 1,4-adduct. The computed overlaps of the HOMO−1_{Az}–$LUMO_{OCO}$ NED interaction for formation of both adducts on a consistent geometry with an average newly forming C/O···N bond length of 1.86 Å amounts $S_{1,5}=0.30$ and $S_{1,4}=0.16$. The larger orbital overlap for the formation of the 1,5-adduct is responsible for the more stabilizing ΔE_{oi} compared to the 1,4-adduct counterpart (Figure 1 b). The NED orbital energy gaps, on the other hand, are identical for the formation of the 1,5- and 1,4-adduct, because the orbital interactions take place between the same molecular orbitals. In addition, the cycloaddition resulting in the 1,5-adduct also has a stronger electrostatic attraction between the more negatively charged nitrogen and the positively charged carbon atom (Scheme 4) and, therefore, a significantly more stabilizing ΔV_{elstat} term (Figure 1 b).

Site-selectivity of asymmetric heteroallenes

After having established that the 1,3-dipolar cycloaddition between **Az** and (hetero)allene preferentially form the 1,5-adduct, we have analyzed the site-selectivity of the asymmetric heteroallenes **CCN**, **NCO**, and **CCO**. First, we discuss the site-selectivity of **CCN** by applying the ASM analysis. From Figure 2 a we can clearly see that the attack of **Az** at the more electropositive CC bond is favored exclusively due to a more stabilizing ΔE_{int} term compared to the attack at the CN bond. The more stabilizing ΔE_{int} for attack at CC compared to CN compensates for the destabilizing ΔE_{strain} for this pathway. Our EDA indicates that the more stabilizing ΔE_{int} term for the attack at CC over CN originates mainly from a more favorable ΔE_{oi} supported by a moderately stronger ΔV_{elstat} (Figure 2 b).

The more stabilizing ΔE_{oi} term for the **Az** attack at CC can exclusively be ascribed to its significantly more favorable inverse electron demand (IED) interaction term (Figure 3 a), which overcomes its less stabilizing NED interaction (Figure 3 b). The IED energy gap for the attack at CC is considerably smaller compared to the attack at CN, 1.7 and 5.0 eV, respectively, while the orbital overlap is also larger for the attack at CC. This manifest in an orbital stabilization term, that is,$10^3\times S^2/\Delta\varepsilon$, of 17.0 and 4.0 for the attack at CC and CN, respectively. In contrast, the NED interaction is slightly weaker for the attack at CC than for CN, due to a larger NED energy gap and a poorer orbital overlap. This, however, can easily be overcome by the much stronger IED interaction, which leads to a more stabilizing ΔE_{oi} and thus a lower reaction barrier for the attack at the CC bond (Figure 2 b).

In the case of the asymmetric linear heteroallene **NCO**, the underlying mechanism behind the preference for the attack at NC over CO is identical to the above discussed **CCN** (Figure S8 a). For heteroallene **CCO**, the ΔE_{strain} for the attack at CC is more destabilizing than for CO, because the terminal carbon atom needs to deform from a trigonal planar to a tetrahedral geometry, which overcomes the more favorable ΔE_{int}, leading to nearly identical reaction barriers (Figure S8 b). But, the cycloaddition at CO is reversible and goes with a positive reaction energy (Table S1 for Gibbs free reaction energies), therefore, the reaction at CC will be preferred thermodynamically. The finding that allenes prefer to undergo cycloadditions at the

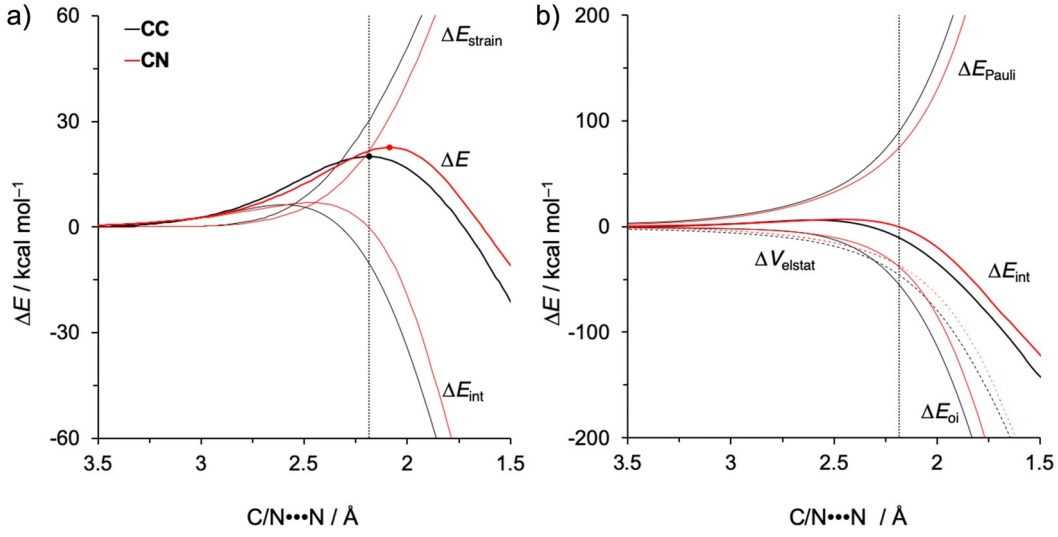

Figure 2. a) Activation strain and b) energy decomposition analysis of site-specific 1,3-dipolar cycloadditions between **Az** and **CCN**, projected onto the average newly forming C/N···N bond, computed at BP86/TZ2P. The vertical dotted line indicates the point along the reaction coordinate at which the average length of newly forming C/N···N bond is 2.19 Å.

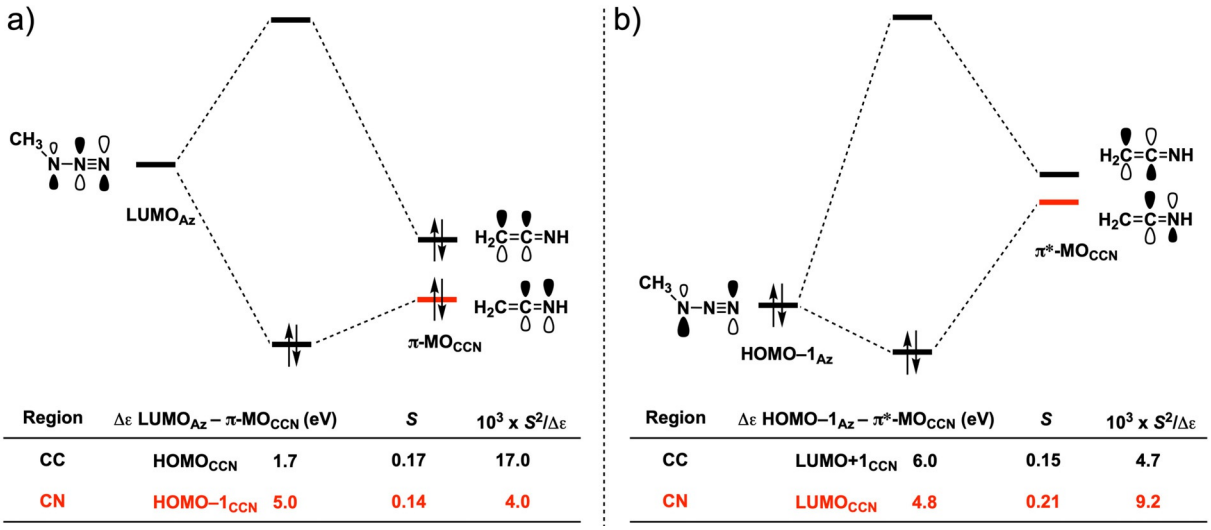

Region	Δε LUMO$_{Az}$ – π-MO$_{CCN}$ (eV)		S	10^3 x S^2/Δε
CC	HOMO$_{CCN}$	1.7	0.17	17.0
CN	HOMO–1$_{CCN}$	5.0	0.14	4.0

Region	Δε HOMO–1$_{Az}$ – π*-MO$_{CCN}$ (eV)		S	10^3 x S^2/Δε
CC	LUMO+1$_{CCN}$	6.0	0.15	4.7
CN	LUMO$_{CCN}$	4.8	0.21	9.2

Figure 3. FMO diagrams with calculated orbital energy gaps and overlaps of a) the IED (LUMO$_{Az}$–π-MO$_{CCN}$) interaction and b) the NED (HOMO−1$_{Az}$–π*-MO$_{CCN}$) interaction for site-specific 1,3-dipolar cycloadditions between **Az** and **CCN** at consistent geometries with the average newly forming C/N···N bond of 2.19 Å computed at BP86/TZ2P.

more electropositive terminal atom is in line with several experimental reports.[7,8,10]

Influence of heteroatoms on the reactivity

In this section, we discuss the effect of heteroatoms on the reactivity of linear allenes towards the 1,3-dipolar cycloaddition with **Az** yielding the 1,5-adduct, by systematically modifying the nature and number of heteroatoms. Upon going from **CCC** to **CCN** and **CCO**, while attacking at the kinetically preferred CC site, the $\Delta E^{\ddagger}$ increases from 19.0 to 20.0 kcal mol^{-1} solely due to a more destabilizing ΔE_{strain} (Figure 4a). Even though **CCC** requires a larger extent of bending over the course of the reaction compared to **CCN** and **CCO** (**CCC**: 24°; **CCN**: 18°; **CCO**: 22°), the difference in ΔE_{strain} can be ascribed to the more rigid heteroallene **CCX** (**X** = **N**, **O**) backbone, which can be reflected by the calculated bending vibrational frequencies of allenes (**CCC**: 361 cm^{-1}; **CCN**: 471 cm^{-1}; **CCO**: 503 cm^{-1}) as well as the analysis of the strain energy upon artificially bending of the heteroallene (Figure S9a). The increased rigidity from **CCC** to **CCN** to **CCO** is due to the increased bond strength between carbon and the heteroatom along the same series.[34] The ΔE_{int} term, on the other hand, shows a trend which is opposite to the strain energy, namely, **CCO** goes with the most stabilizing interaction energy followed by **CCN** and **CCC**. This trend in interaction energy is exclusively determined by the orbital interactions (see Figure S9b for EDA diagrams), which, in turn, can be traced to a less stable LUMO$_{allene}$ going from **CCO**

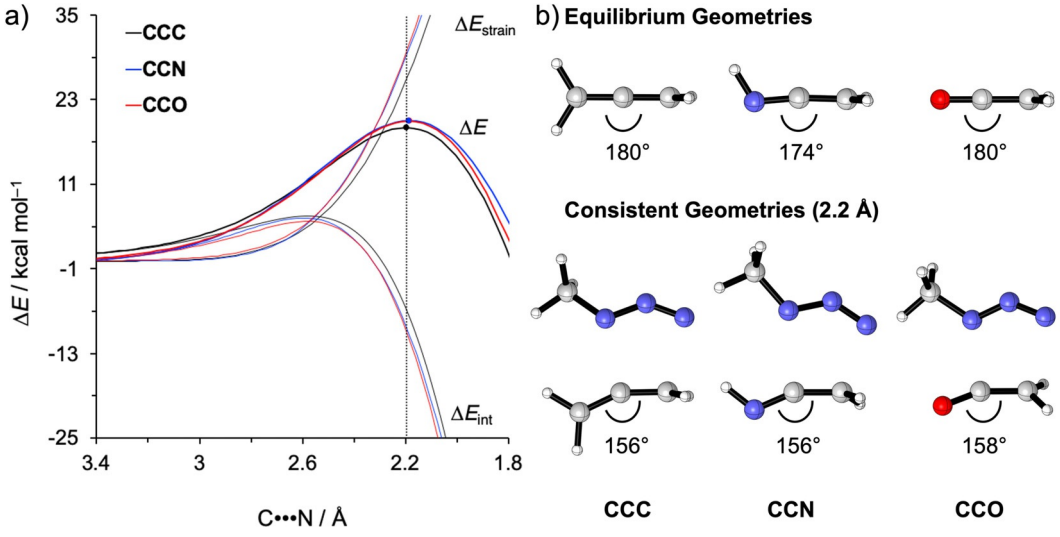

Figure 4. a) Activation strain analysis for the 1,3-dipolar cycloadditions between **Az** and **CCC**, **CCN**, and **CCO** attacking at the CC site and b) equilibrium geometries of the allene and respective consistent geometries with the average newly forming C/N···N bond of 2.20 Å with internal bending angles [°] computed at BP86/TZ2P.

to **CCN** and **CCC** (−2.4, −1.5, and −0.9 eV, respectively), and, therefore, a larger HOMO−1_{Az}–$LUMO_{allene}$ energy gap. This trend in ΔE_{int} term, however, is overruled by the larger differences in ΔE_{strain}.

For the series **CCO**, **NCO**, and **OCO**, **Az** attacks at different sites, namely, CC, NC, and OC, respectively, but the neighboring heteroatom is always oxygen. Along this series, the $\Delta E^{\ddagger}$ systematically increases (Table 1), due to a less stabilizing ΔE_{oi} (Figure S10). Similar to the analysis of the site-selectivity of the asymmetric heteroallenes (Figure 3), going from CC to the hetero double bonds NC and OC causes a remarkably destabilized IED interaction ($LUMO_{Az}$–$HOMO_{allene}$), due to the increased IED orbital energy gap supported by less efficient orbital overlap (Figure S11). This exact rationale also holds for the comparison of **CCN** and **NCN** (Figure S12).

Summarizing, we have analyzed and compared the 1,3-dipolar cycloaddition reactivity of linear (hetero)allenes with **Az**, which is all cases prefers to form the 1,5-adduct. The archetypal allene, **CCC**, is the most reactive. By introducing a heteroatom, the heteroallene becomes less reactive due to the increased rigidity of the **CCX** (**X** = **N**, **O**) backbone. Additionally, a second heteroatom diminishes the stabilizing ΔE_{oi}, making them even less reactive towards **Az**.

1,3-Dipolar cycloaddition of cyclic allenes

At last, we also analyzed and compared the 1,3-dipolar cycloaddition reactions between methyl azide (**Az**) and a series of cyclic allenes, namely, 1,2-cyclooctadiene (**C8**), 1,2-cycloheptadiene (**C7**), and 1,2-cyclohexadiene (**C6**) as well as propadiene (**L3**), the most reactive linear allene (vide supra). These cyclic allenes have all been synthesized and featured in cycloaddition reactions.[13]

Figure 5 shows the transition state structures of the 1,3-dipolar cycloadditions of **Az** with the linear allene (**Az**-**L3**) and the cyclic allenes (**Az**-**C8**–**Az**-**C6**). The transition structures are concerted asynchronous and become earlier, with regard to the average forming bond distances, as the ring size of the cyclic allene decreases. The cycloaddition of the linear **L3** is predicted to proceed with the highest reaction barrier ($\Delta E^{\ddagger}$ = 19.0 kcal mol^{-1}) and has the least favorable reaction energy (ΔE_{rxn} = −34.0 kcal mol^{-1}). The reaction barrier height decreases along the series **L3** > **C8** > **C7** > **C6**, and the cycloaddition reaction becomes more exergonic when going from **L3** to **C6**, which is in line with the Hammond–Leffler postulate[35] (Figure S13). The computed trends at BP86/TZ2P agree well with those calculated at BP86-D3(BJ)/TZ2P//BP86/TZ2P and M06-2X/TZ2P//BP86/TZ2P, as well as when solvent effects are included at COSMO(toluene)BP86/TZ2P//BP86/TZ2P (Table S2).

In order to understand the intrinsic differences in reactivity between linear and cyclic allenes in the 1,3-dipolar cycloaddition with **Az**, we performed an ASM analysis. Figure 6a graphically represents how the ΔE_{strain} and ΔE_{int} components evolve along the reaction coordinate for 1,3-dipolar cycloadditions of **Az** with **L3** and **C8**–**C6**. Surprisingly, the origin of the increased reactivity as the ring size of allene decreases can be entirely attributed to the differences in ΔE_{int}, which becomes more stabilizing from **L3** to **C6** (Figure 6a). The total ΔE_{strain} for all studied allenes are nearly identical (Figure 6a). As expected upon decreasing the size of the ring, the cyclic allene becomes more predistorted towards the cycloaddition reaction with **Az**, which leads to a smaller contribution of the cyclic allene to the total ΔE_{strain}, consistent with the earlier literature.[13f] The contribution of the 1,3-dipole **Az** to the total ΔE_{strain}, however, is more destabilizing for **C6** than for **L3** (Figure S14), due to the fact that the more reactive allenes (vide infra) deform **Az** to a larger degree (Figure S15).

The origin of the differences in ΔE_{int} was uncovered by means of the EDA method, and the results are shown in Figure 6b. It is apparent that the ΔE_{oi} is the major contributor to the trend in ΔE_{int}, guided by a smaller contribution of ΔV_{elstat}. The ΔE_{Pauli} shows a reverse trend, and, therefore, is not responsible for the trend in ΔE_{int}. To further probe the key orbital interactions, that cause this difference in ΔE_{oi}, involved in the 1,3-dipolar cycloadditions of **Az** with **L3** and **C8**–**C6**, we analyzed the FMOs participating in these interactions on consistent geometries with an average newly forming C···N bond of 2.48 Å (Figure 7).

The FMOs participating in the NED and IED reveal that the more stabilizing orbital interactions when going from **L3** to **C8**

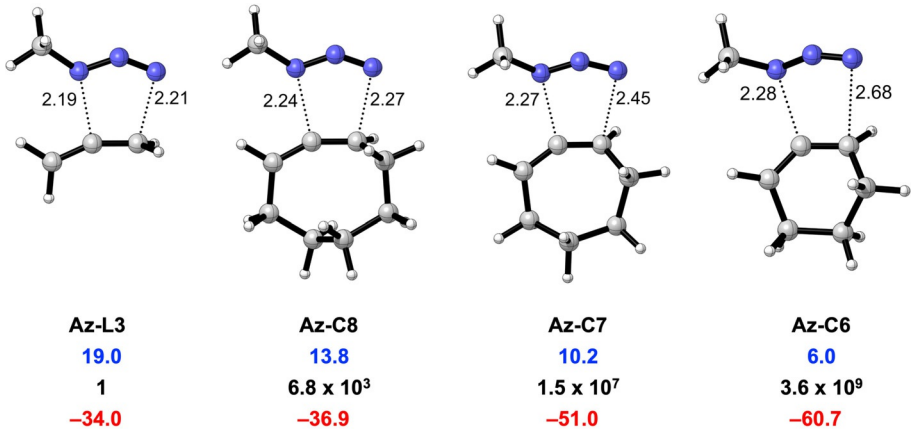

Figure 5. Transition structures with forming bond lengths [Å], computed reaction barriers ($\Delta E^{\ddagger}$ [kcal mol^{-1}], blue) with relative reaction rate constants (k_{rel}, black), and reaction energies (ΔE_{rxn} [kcal mol^{-1}], red) for 1,3-dipolar cycloadditions of **Az** with **L3** and **C8**–**C6** computed at BP86/TZ2P.

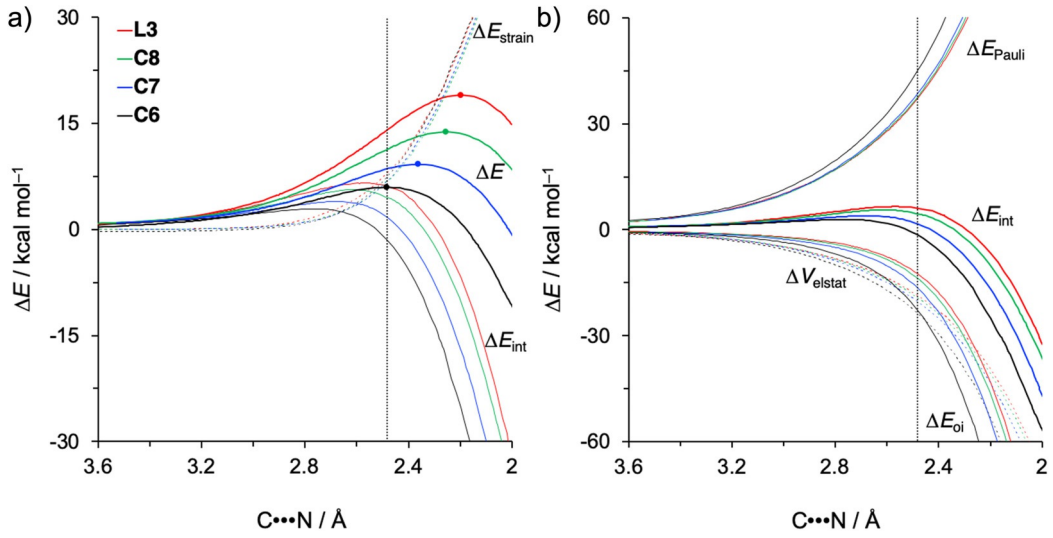

Figure 6. a) Activation strain and b) energy decomposition analysis of 1,3-dipolar cycloadditions of **Az** with **L3** and **C8**–**C6**, projected onto the average newly forming C···N bond, computed at BP86/TZ2P. The vertical dotted line indicates the point along the reaction coordinate where the average newly forming C···N bond is 2.48 Å.

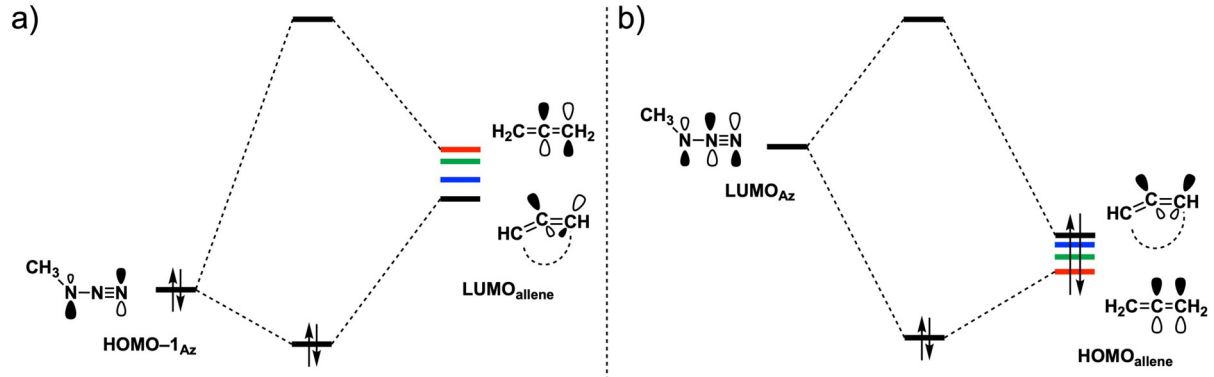

Compound	Δε HOMO–1$_{Az}$–LUMO$_{allene}$ (eV)	*S*
L3	6.4	0.15
C8	6.1	0.15
C7	5.4	0.15
C6	4.8	0.15

Compound	Δε LUMO$_{Az}$–HOMO$_{allene}$ (eV)	*S*
L3	3.7	0.10
C8	3.2	0.09
C7	2.9	0.10
C6	2.7	0.12

Figure 7. FMO diagrams with calculated key orbital energy gaps and overlaps of a) the NED (HOMO−1$_{Az}$–LUMO$_{allene}$) interaction and b) the IED (LUMO$_{Az}$–HOMO$_{allene}$) interaction for 1,3-dipolar cycloadditions between **Az** with **L3** and **C8**–**C6** at consistent geometries with the average newly forming C···N bond of 2.48 Å computed at BP86/TZ2P.

to **C6** are exclusively determined by a reduction in orbital energy gap (Figure 7). The NED interaction between **Az** and **L3** and **C8**–**C6** occurs between the HOMO−1$_{Az}$ and LUMO$_{allene}$ (Figure 7a). The least reactive allene **L3** has the largest and least favorable NED orbital energy gap ($\Delta\varepsilon = 6.4$ eV). As the ring size decreases from **L3** to **C8** to **C6**, the NED orbital energy gap continuously decreases from 6.4 to 4.8 eV. The orbital overlap in the NED interaction are identical for all reactions ($S = 0.15$). The IED interaction takes place between the LUMO$_{Az}$ and HOMO$_{allene}$ (Figure 7b). Again, **L3** has the largest and, therefore, least favorable IED orbital energy gap ($\Delta\varepsilon =$ 3.7 eV). The IED gap also systematically decreases from 3.7 eV for **L3** to 2.7 eV for **C6**. The increasingly stabilizing ΔE_{oi} term (Figure 6b), as the ring size of allene decreases, therefore, is a direct result of the diminishing energy gap for both the NED and IED interaction, resulted from the continuously stabilizing LUMO and destabilizing HOMO of allene (Figures 7 and S16).

In order to quantify the effect of allene predistortion on the HOMO and LUMO, we chose to bent our model system **L3**. Figure 8a shows the optimized undistorted structure (top) and the distorted, bent, structures of **L3** (middle and bottom). Bending of the allene backbone causes a loss in orthogonality of the two adjacent π systems, because it is accompanied with a twist in the structure, reducing the dihedral angle from 90°,

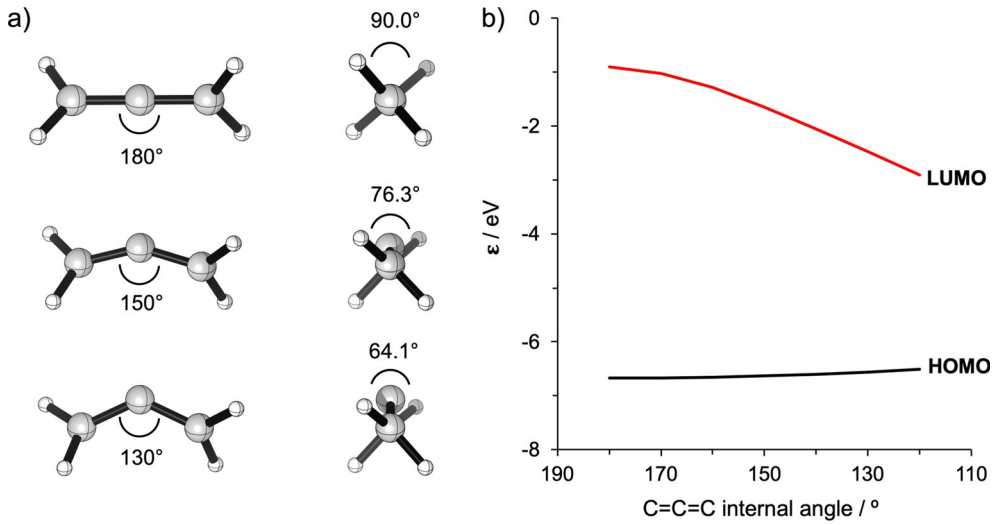

Figure 8. a) Front and right-side views of the pristine and constrained optimized structures of **L3**. b) FMO energies associated with the internal angle computed at BP86/TZ2P.

for the linear allene, to 64.1°, for the 130° bent allene. This observation not only holds for **L3**, but also for the cyclic allenes **C6**–**C8** (Figure S17) and is in line with earlier reported literature.[13g] As the backbone of **L3** becomes distorted, the LUMO is stabilized while the HOMO is destabilized (Figure 8b).

Detailed Kohn–Sham molecular orbital (KS-MO) analysis of the formation of the HOMO and LUMO of the undistorted (linear) and distorted (bent to 130°) $H_2C{=}C{=}CH_2$ (**L3**), in terms of an $H_2C{=}C{:}$ and a $:CH_2$ fragment, is shown in Figure 9. For the archetypal **L3** (Figure 9a), one LUMO (the bold LUMOs in Figure 9) is solely formed by the π* orbital of $H_2C{=}C{:}$, whereas the other degenerate LUMO, which is orthogonal to the former, is a result of the antibonding combination of the *p* orbitals of two individual fragments. Furthermore, the HOMO (the bold HOMOs in Figure 9) originates from the antibonding combination between the π orbital of $H_2C{=}C{:}$ and the C–H σ orbital of $:CH_2$, meanwhile the other degenerate HOMO is the bonding combination of the *p* orbitals of both fragments. When **L3** is bent to 130° (Figure 9b), the π* orbital of $H_2C{=}C{:}$ has an in-phase overlap with the σ* orbital of $:CH_2$ which leads to a stabilization of the LUMO. In addition, due to the prior mentioned twisting effect, the fragment p orbitals mix into the LUMO which results in the additional stabilization. The HOMO, on the other hand, is stabilized due to the decreased antibonding π–σ overlap owing to the bending and twisting of the backbone, but, at the same time, obtains a slightly stronger destabilization from the mixing of the fragmental p orbitals. This destabilization effect overcomes the stabilizing counterpart, resulting in the overall destabilization of the HOMO.

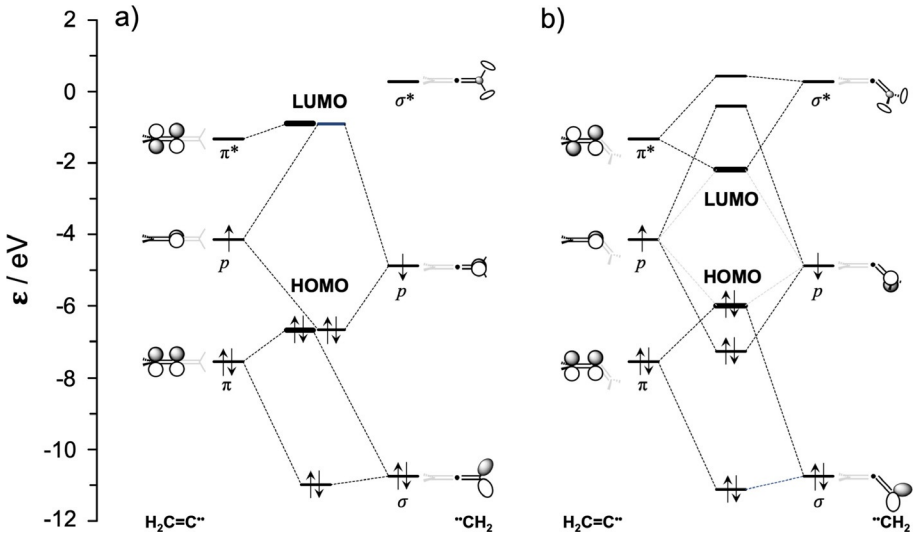

Figure 9. Diagrams for the Kohn–Sham MO analyses of a) the archetypal and b) 130° bent **L3**, where the fragments are $H_2C{=}C{:}$ and $:CH_2$ computed at BP86/TZ2P.

These analyses were further verified by investigating both the pure bending (no twisting) or twisting (no bending) of **L3**. Solely bending **L3** and maintaining orthogonality of the structure stabilizes the LUMO due to the enhanced π^*–σ^* overlap and also stabilizes the HOMO because of the decreased π–σ overlap (Figure S18). On the other hand, solely twisting **L3** and maintaining a linear backbone induces a stabilization of the LUMO, because of an in-phase mixing between the π^* and *p* orbitals of the fragments, and a significantly destabilization of the HOMO, due to the mixing between the π and p orbitals (Figure S19).

Conclusions

1,3-Dipolar cycloadditions of linear allenes and heteroallenes with methyl azide (**Az**) favor the formation of the 1,5-adduct over the 1,4-adduct. In addition, bond formation to the asymmetric heteroallene is preferred at the more electropositive terminal atom. This process becomes less reactive as the number of heteroatoms in the allene increases. Cyclic allenes experience a significant rate enhancement compared to their linear allene counterparts. These findings emerge from our quantum chemical study based on density functional theory calculations.

Our activation strain analyses furthermore identified that the site-selective preference for the 1,5-adduct compared to the 1,4-adduct is exclusively determined by a more favorable orbital overlap and thus more stabilizing orbital interactions between the reactants. Furthermore, in the case of the asymmetric heteroallenes, the preference for attacking at the more electropositive atoms is caused by a significantly stronger inverse electron demand (IED) orbital interaction. This is due to the fact that double bonds involving more electropositive atoms have lower-lying acceptor orbitals, leading to smaller IED energy gaps and, thus, more stabilizing orbital interactions with **Az**. The archetypal allene, propadiene (**CCC**) was found to be the most reactive linear allene. Introducing a heteroatom to **CCC** makes the allene less reactive, due to a more destabilizing ΔE_{strain}, originating from a more rigid backbone, as well as less stabilizing orbital interactions.

The enhanced reactivity of cyclic allenes with respect to linear ones originates from an enhancement of donor–acceptor orbital interactions, which become more stabilizing as the ring size of the cyclic allene decreases, and not from a previously reported reduced activation strain. Our activation strain analyses reveal that, in smaller rings, the allene moiety is more bent; this goes with a smaller HOMO–LUMO gap in the π-electron system and, hence, with the aforementioned stabilization of the transition state by stronger donor–acceptor orbital interactions.

Acknowledgements

This work was supported by the Netherlands Organization for Scientific Research (NWO), the China Scholarship Council (CSC), and the Dutch Astrochemistry Network (DAN-II). We thank SURFsara for use of the Cartesius supercomputer.

Conflict of interest

The authors declare no conflict of interest.

Keywords: 1,3-dipolar cycloadditions · activation strain model · allenes · density functional theory calculations · reactivity

[1] a) S. Yu, S. Ma, *Angew. Chem. Int. Ed.* **2012**, *51*, 3074 – 3112; *Angew. Chem.* **2012**, *124*, 3128 – 3167; b) A. Hoffmann-Röder, N. Krause, *Angew. Chem. Int. Ed.* **2004**, *43*, 1196 – 1216; *Angew. Chem.* **2004**, *116*, 1216 – 1236; c) N. Krause, A. S. K. Hashmi, *Modern Allene Chemistry*, Wiley-VCH, Weinheim, **2004**; d) T. M. V. D. Pinho e Melo, *Curr. Org. Chem.* **2009**, *13*, 1406 – 1431; e) T. M. V. D. Pinho e Melo, *Monatsh. Chem.* **2011**, *142*, 681 – 697; f) A. L. Cardoso, *Curr. Org. Chem.* **2019**, *23*, 3064 – 3134.

[2] F. Scheufler, M. E. Maier, *Eur. J. Org. Chem.* **2000**, 3945 – 3948.

[3] A. Padwa, D. N. Kline, K. F. Koehler, M. Matzinger, M. K. Venkatramanan, *J. Org. Chem.* **1987**, *52*, 3909 – 3917.

[4] a) G. Himbert, L. Henn, *Angew. Chem. Int. Ed. Engl.* **1982**, *21*, 620; *Angew. Chem.* **1982**, *94*, 631; b) G. Himbert, D. Fink, K. Diehl, P. Rademacher, A. J. Bittner, *Chem. Ber.* **1989**, *122*, 1161 – 1173.

[5] K. S. Feldman, M. R. Iyer, *J. Am. Chem. Soc.* **2005**, *127*, 4590 – 4591.

[6] a) L. S. Trifonov, A. S. Orahovats, *Helv. Chim. Acta* **1989**, *72*, 59 – 64; b) Y. Schmidt, J. K. Lam, H. V. Pham, K. N. Houk, C. D. Vanderwal, *J. Am. Chem. Soc.* **2013**, *135*, 7339 – 7348; c) G. Cheng, X. He, L. Tian, J. Chen, C. Li, X. Jia, J. Li, *J. Org. Chem.* **2015**, *80*, 11100 – 11107; d) J. K. Lam, Y. Schmidt, C. D. Vanderwal, *Org. Lett.* **2012**, *14*, 5566 – 5569; e) K. S. Feldman, D. K. Hester, C. S. López, O. N. Faza, *Org. Lett.* **2008**, *10*, 1665 – 1668; f) K. S. Feldman, D. K. Hester, M. R. Iyer, P. J. Munson, C. Silva López, O. N. Faza, *J. Org. Chem.* **2009**, *74*, 4958 – 4974; g) K. S. Feldman, M. R. Iyer, C. Silva López, O. N. Faza, *J. Org. Chem.* **2008**, *73*, 5090 – 5099; h) K. S. Feldman, I. Y. Gonzalez, C. M. Glinkerman, *J. Am. Chem. Soc.* **2014**, *136*, 15138 – 15141; i) K. S. Feldman, I. Y. Gonzalez, C. M. Glinkerman, *J. Org. Chem.* **2015**, *80*, 11849 – 11862.

[7] a) C. Larksarp, O. Sellier, H. Alper, *J. Org. Chem.* **2001**, *66*, 3502 – 3506; b) M. Alajarin, B. Bonillo, M.-M. Ortin, R.-A. Orenes, A. Vidal, *Org. Biomol. Chem.* **2011**, *9*, 6741 – 6749; c) W. J. Kauffman, *J. Org. Chem.* **1970**, *35*, 4244 – 4245.

[8] a) X.-L. Huang, L. He, P.-L. Shao, S. Ye, *Angew. Chem. Int. Ed.* **2009**, *48*, 192 – 195; *Angew. Chem.* **2009**, *121*, 198 – 201; b) T.-Y. Jian, X.-Y. Chen, L.-H. Sun, S. Ye, *Org. Biomol. Chem.* **2013**, *11*, 158 – 163; c) M. Schmittel, H. von Seggern, *J. Am. Chem. Soc.* **1993**, *115*, 2165 – 2177; d) P.-L. Shao, X.-Y. Chen, S. Ye, *Angew. Chem. Int. Ed.* **2010**, *49*, 8412 – 8416; *Angew. Chem.* **2010**, *122*, 8590 – 8594; e) M. Presset, K. Mohana, M. Hamann, Y. Coquerel, J. Rodriguez, *Org. Lett.* **2011**, *13*, 4124 – 4127.

[9] a) J. Světlík, J. Leško, A. Martvoň, *Monatsh. Chem.* **1980**, *111*, 635 – 642; b) W.-P. Yen, F.-C. Kung, F. F. Wong, *Eur. J. Org. Chem.* **2016**, 2328 – 2335.

[10] a) K. M. Oberg, T. Rovis, *J. Am. Chem. Soc.* **2011**, *133*, 4785 – 4787; b) Z. Zheng, Y. Cao, D. Zhu, Z. Wang, K. Ding, *Chem. Eur. J.* **2019**, *25*, 9491 – 9497.

[11] a) L.-L. Zhao, S.-Y. Wang, X.-P. Xu, S.-J. Ji, *Chem. Commun.* **2013**, *49*, 2569 – 2571; b) C.-X. Guo, W.-Z. Zhang, N. Zhang, X.-B. Lu, *J. Org. Chem.* **2017**, *82*, 7637 – 7642; c) F. Murillo, J. Barroso, M. G. de los Santos, G. Ávila, S. Pan, M. A. Fernández-Herrera, G. Merino, *J. Org. Chem.* **2018**, *83*, 13045 – 13050.

[12] a) R. O. Angus, M. W. Schmidt, R. P. Johnson, *J. Am. Chem. Soc.* **1985**, *107*, 532 – 537; b) R. P. Johnson, *Chem. Rev.* **1989**, *89*, 1111 – 1124; c) K. J. Daoust, S. M. Hernandez, K. M. Konrad, I. D. Mackie, J. Winstanley, R. P. Johnson, *J. Org. Chem.* **2006**, *71*, 5708 – 5714.

[13] a) P. Mohanakrishnan, S. R. Tayal, R. Vaidyanathaswamy, D. A. Devaprabhakara, *Tetrahedron Lett.* **1972**, *13*, 2871 – 2872; b) A. T. Bottini, L. L. Hilton, *Tetrahedron* **1975**, *31*, 2003 – 2004; c) M. Balci, W. M. Jones, *J. Am. Chem. Soc.* **1980**, *102*, 7607 – 7608; d) M. Nendel, L. M. Tolbert, L. E. Herring, M. N. Islam, K. N. Houk, *J. Org. Chem.* **1999**, *64*, 976 – 983; e) V. A.

Lofstrand, F. G. West, *Chem. Eur. J.* **2016**, *22*, 10763 – 10767; f) J. S. Barber, E. D. Styduhar, H. V. Pham, T. C. McMahon, K. N. Houk, N. K. Garg, *J. Am. Chem. Soc.* **2016**, *138*, 2512 – 2515; g) J. S. Barber, M. M. Yamano, M. Ramirez, E. R. Darzi, R. R. Knapp, F. Liu, K. N. Houk, N. K. Garg, *Nat. Chem.* **2018**, *10*, 953 – 960.

[14] a) R. Manova, T. A. van Beek, H. Zuilhof, *Angew. Chem. Int. Ed.* **2011**, *50*, 5428 – 5430; *Angew. Chem.* **2011**, *123*, 5540 – 5542; b) S. S. van Berkel, S. Brauch, L. Gabriel, M. Henze, S. Stark, D. Vasilev, L. A. Wessjohann, M. Abbas, B. Westermann, *Angew. Chem. Int. Ed.* **2012**, *51*, 5343 – 5346; *Angew. Chem.* **2012**, *124*, 5437 – 5441; c) C. Wendeln, I. Singh, S. Rinnen, C. Schulz, H. F. Arlinghaus, G. A. Burley, B. J. Ravoo, *Chem. Sci.* **2012**, *3*, 2479 – 2484; d) S. H. Lee, O. K. Park, J. Kim, K. Shin, C. G. Pack, K. Kim, G. Ko, N. Lee, S.-H. Kwon, T. Hyeon, *J. Am. Chem. Soc.* **2019**, *141*, 13829 – 13840; e) J. Escorihuela, A. Das, W. J. E. Looijen, F. L. van Delft, A. J. A. Aquino, H. Lischka, H. Zuilhof, *J. Org. Chem.* **2018**, *83*, 244 – 252.

[15] a) A. Rastelli, M. Bagatti, R. Gandolfi, *Tetrahedron* **1994**, *50*, 5561 – 5568; b) A. Rastelli, M. Bagatti, R. Gandolfi, *J. Am. Chem. Soc.* **1995**, *117*, 4965 – 4975; c) M. Manoharan, P. Venuvanalingam, *J. Chem. Soc. Perkin Trans. 2* **1996**, 1423 – 1427; d) A. B. G. Pérez, A. B. González Pérez, J. A. Souto, C. S. López, Á. R. de Lera, *Eur. J. Org. Chem.* **2011**, 2933 – 2939; e) C. S. López, O. N. Faza, K. S. Feldman, M. R. Iyer, D. K. Hester, *J. Am. Chem. Soc.* **2007**, *129*, 7638 – 7646.

[16] a) C. Wentrup, G. Gross, A. Maquestiau, R. Flammang, *Angew. Chem. Int. Ed. Engl.* **1983**, *22*, 542 – 543; *Angew. Chem.* **1983**, *95*, 551 – 551; b) W. R. Moore, W. R. Moser, *J. Am. Chem. Soc.* **1970**, *92*, 5469 – 5474; c) I. Quintana, D. Peña, D. Pérez, E. Guitián, *Eur. J. Org. Chem.* **2009**, 5519 – 5524; d) G. Wittig, P. Fritze, *Angew. Chem. Int. Ed. Engl.* **1966**, *5*, 846; *Angew. Chem.* **1966**, *78*, 905; e) J. D. Price, R. P. Johnson, *Tetrahedron Lett.* **1986**, *27*, 4679 – 4682; f) E. T. Marquis, P. D. Gardner, *Tetrahedron Lett.* **1966**, *7*, 2793 – 2798.

[17] a) N. J. Agard, J. A. Prescher, C. R. Bertozzi, *J. Am. Chem. Soc.* **2004**, *126*, 15046 – 15047; b) S. T. Laughlin, J. M. Baskin, S. L. Amacher, C. R. Bertozzi, *Science* **2008**, *320*, 664 – 667; c) M. F. Debets, C. W. J. van der Doelen, F. P. J. T. Rutjes, F. L. van Delft, *ChemBioChem* **2010**, *11*, 1168 – 1184.

[18] a) R. Huisgen, *Angew. Chem. Int. Ed. Engl.* **1963**, *2*, 565 – 598; *Angew. Chem.* **1963**, *75*, 604 – 637; b) F. Himo, T. Lovell, R. Hilgraf, V. V. Rostovtsev, L. Noodleman, K. B. Sharpless, V. V. Fokin, *J. Am. Chem. Soc.* **2005**, *127*, 210 – 216; c) V. V. Rostovtsev, L. G. Green, V. V. Fokin, K. B. Sharpless, *Angew. Chem. Int. Ed.* **2002**, *41*, 2596 – 2599; *Angew. Chem.* **2002**, *114*, 2708 – 2711; d) C. W. Tornøe, C. Christensen, M. Meldal, *J. Org. Chem.* **2002**, *67*, 3057 – 3064.

[19] a) P. Vermeeren, S. C. C. van der Lubbe, C. Fonseca Guerra, F. M. Bickelhaupt, T. A. Hamlin, *Nat. Protoc.* **2020**, *15*, 649 – 667; b) F. M. Bickelhaupt, K. N. Houk, *Angew. Chem. Int. Ed.* **2017**, *56*, 10070 – 10086; *Angew. Chem.* **2017**, *129*, 10204 – 10221; c) D. H. Ess, K. N. Houk, *J. Am. Chem. Soc.* **2008**, *130*, 10187 – 10198; d) L. P. Wolters, F. M. Bickelhaupt, *Wiley Interdiscip. Rev.: Comput. Mol. Sci.* **2015**, *5*, 324 – 343; e) I. Fernández, F. M. Bickelhaupt, *Chem. Soc. Rev.* **2014**, *43*, 4953 – 4967; f) W.-J. van Zeist, F. M. Bickelhaupt, *Org. Biomol. Chem.* **2010**, *8*, 3118 – 3127.

[20] a) F. M. Bickelhaupt, E. J. Baerends in *Reviews in Computational Chemistry* (Eds.: K. B. Lipkowitz, D. B. Boyd), Wiley, Hoboken, **2000**, pp. 1 – 86; b) R. van Meer, O. V. Gritsenko, E. J. Baerends, *J. Chem. Theory Comput.* **2014**, *10*, 4432 – 4441; c) L. Zhao, M. von Hopffgarten, D. M. Andrada, G. Frenking, *WIREs Comput. Mol. Sci.* **2018**, *8*, e1345.

[21] a) B. J. Levandowski, T. A. Hamlin, F. M. Bickelhaupt, K. N. Houk, *J. Org. Chem.* **2017**, *82*, 8668 – 8675; b) T. A. Hamlin, B. J. Levandowski, A. K. Narsaria, K. N. Houk, F. M. Bickelhaupt, *Chem. Eur. J.* **2019**, *25*, 6342 – 6348.

[22] a) G. te Velde, F. M. Bickelhaupt, E. J. Baerends, C. Fonseca Guerra, S. J. A. van Gisbergen, J. G. Snijders, T. Ziegler, *J. Comput. Chem.* **2001**, *22*, 931 – 967; b) C. Fonseca Guerra, J. G. Snijders, G. te Velde, E. J. Baerends, *Theor. Chem. Acc.* **1998**, *99*, 391 – 403; c) *ADF*, SCM Theoretical Chemistry; Vrije Universiteit, Amsterdam (The Netherlands), **2017**; http://www.scm.com.

[23] a) A. D. Becke, *Phys. Rev. A* **1988**, *38*, 3098 – 3100; b) J. P. Perdew, *Phys. Rev. B* **1986**, *33*, 8822 – 8824.

[24] E. van Lenthe, E. J. Baerends, *J. Comput. Chem.* **2003**, *24*, 1142 – 1156.

[25] a) A. Talbot, D. Devarajan, S. J. Gustafson, I. Fernández, F. M. Bickelhaupt, D. H. Ess, *J. Org. Chem.* **2015**, *80*, 548 – 558; b) T. A. Hamlin, D. Svatunek, S. Yu, L. Ridder, I. Infante, L. Visscher, F. M. Bickelhaupt, *Eur. J. Org. Chem.* **2019**, 378 – 386; c) S. Yu, H. M. de Bruijn, D. Svatunek, T. A. Hamlin, F. M. Bickelhaupt, *ChemistryOpen* **2018**, *7*, 995 – 1004.

[26] a) S. Grimme, S. Ehrlich, L. Goerigk, *J. Comput. Chem.* **2011**, *32*, 1456 – 1465; b) J. G. Brandenburg, J. E. Bates, J. Sun, J. P. Perdew, *Phys. Rev. B* **2016**, *94*, 115144.

[27] a) Y. Zhao, D. G. Truhlar, *J. Chem. Phys.* **2006**, *125*, 194101; b) Y. Zhao, D. G. Truhlar, *Theor. Chem. Acc.* **2008**, *120*, 215 – 241.

[28] a) A. Klamt, G. Schüürmann, *J. Chem. Soc. Perkin Trans. 2* **1993**, 799 – 805; b) A. Klamt, *J. Phys. Chem.* **1995**, *99*, 2224 – 2235; c) A. Klamt, V. Jonas, *J. Chem. Phys.* **1996**, *105*, 9972; d) C. C. Pye, T. Ziegler, *Theor. Chem. Acc.* **1999**, *101*, 396 – 408.

[29] a) W.-J. van Zeist, C. Fonseca Guerra, F. M. Bickelhaupt, *J. Comput. Chem.* **2008**, *29*, 312 – 315; b) X. Sun, T. M. Soini, J. Poater, T. A. Hamlin, F. M. Bickelhaupt, *J. Comput. Chem.* **2019**, *40*, 2227 – 2233.

[30] C. Y. Legault, *CYLview*, 1.0b; Université de Sherbrooke, Sherbrooke (QC, Canada), **2009**; http://www.cylview.org.

[31] D. Svatunek, N. Houszka, T. A. Hamlin, F. M. Bickelhaupt, H. Mikula, *Chem. Eur. J.* **2019**, *25*, 754 – 758.

[32] T. A. Albright, J. K. Burdett, M.-H. Whangbo, *Orbital Interactions in Chemistry*, 2nd ed., Wiley, Hoboken, **2013**.

[33] C. Fonseca Guerra, J.-W. Handgraaf, E. J. Baerends, F. M. Bickelhaupt, *J. Comput. Chem.* **2004**, *25*, 189 – 210.

[34] Y.-R. Luo, *Comprehensive Handbook of Chemical Bond Energies*, CRC Press, Boca Raton, **2007**.

[35] G. S. Hammond, *J. Am. Chem. Soc.* **1955**, *77*, 334 – 338.

Manuscript received: February 17, 2020
Revised manuscript received: March 25, 2020
Accepted manuscript online: March 27, 2020
Version of record online: August 7, 2020